Delft University of Technology

Surface effects of molten slag spills on calcium aluminate cement paste

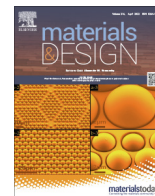Mendonça Filho, F.F.; Rodriguez, C. Romero; Schlangen, E.; Copuroglu, O.

Important note
To cite this publication, please use the final published version (if applicable).
Please check the document version above.

Surface effects of molten slag spills on calcium aluminate cement paste

F.F. Mendonça Filho *, C. Romero Rodriguez, E. Schlangen, O. Çopuroğlu

Materials & Environment, Faculty of Civil Engineering and Geosciences, Delft University of Technology, Stevinweg 1, Delft, Netherlands

HIGHLIGHTS

- Heating samples in an oven is a poor method to simulate concrete exposed to industrial spills.
- Pouring slag at 1500 °C in cement samples simulates a factory setting much better.
- The thermo-mechanical damage depends on saturation and porosity.
- Thermo-chemical alterations varied based on Si diffusion and vapour absorption.

GRAPHICAL ABSTRACT
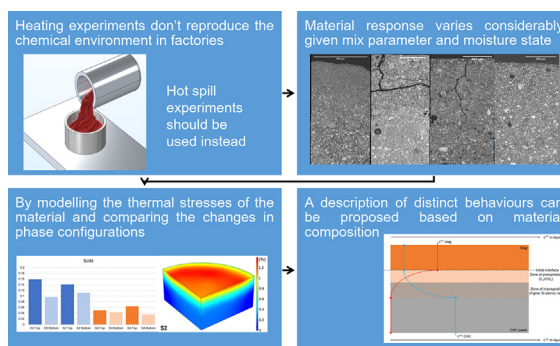
ARTICLE INFO

ABSTRACT

Industries such as metal, ceramics and petrochemicals suffer from high temperature spills. Such events exert a unique form of loading in concrete structures that cannot be accurately simulated by heating of samples in an oven. Calcium aluminate cement (CAC) based concrete is the industry standard for such environment, and while much is known regarding its heating, literature considering hot spills on concrete surfaces is scarce. In this paper, slag is heated up to the same temperature as in a steel factory and then poured on top of cement paste samples with W/C ratios of 0.20 and 0.40. A combination of FEM, TGA, XRD and SEM/EDS was used to investigate the effects of hot spill on the samples. The rapid expansion caused by the thermal shock generated cracks in only some of the samples, while the high temperature environment and unidirectional escape of water caused chemical changes in all samples.

1. Introduction

Industries such as metal, ceramics and petrochemicals suffer from spillages in controlled environments of factories. While rarely a danger to workers, these spills cause considerable damage to the infrastructure of the factories and demand constant repair work, which interrupts production and leads to costly maintenance campaigns. This is not cost efficient or environmentally sustainable, thus mitigation strategies must be pursued.

The key concept towards designing cost effective, environmentally sustainable structures for the harsh setting of such industries is their durability.Yet, Portland cement (PC) based concrete is known to behave poorly against high temperature [1,2], losing most of its capacity at temperatures above 600 °C [3]. This is due the decomposition of the two main hydration products, portlandite (CH) and calcium silicate hydrate ($C-S-H$). In the range of 300 °C to 700 °C, these compounds become lime and calcium silicates respectively [4]. At this point, the binding property is lost and the material can no longer fulfil its structural function.

Alternatively, calcium aluminate cement (CAC) retains mechanical properties much better when exposed to elevated temperature [5], which makes it the most common binder used for refractory

* Corresponding author.
E-mail address: f.filho@tudelft.nl (F.F. Mendonça Filho).

F.F. Mendonça Filho, C. Romero Rodriguez, E. Schlangen et al.

Materials & Design 217 (2022) 110623

applications [6]. This is explained by the different hydration products formed, namely CAH_{10} and C_2AH_8. From room temperature to 200 °C, these meta-stable products will achieve a stable form of hydrogarnet (C_3AH_6) and generate alumina gel (AH_3) and water through well-known reactions [7]. From 300 °C to 1000 °C, loss of the chemically bound water on the stable products occur, decreasing mechanical properties at a slower pace than in PC [8]. Above 1000 °C, formation of calcium aluminate (CA), calcium dialuminate (CA_2) and calcium hexa-aluminate (CA_6, >1400 °C) will create a network of sintered products that improve the mechanical properties of the material, resulting in a even stronger binder compared to pristine CAC [9].

However, improvement in durability requires clear understanding of the deterioration mechanisms taking place at a material level. But most high temperature studies on concrete are executed by the steadily heating up samples [10–14], which would not account to mechanisms related to contact with high temperature spillage. In case of such an event, nonlinear rapid heating is followed by slow cooling while the material is in contact with specific chemicals. Therefore, there is a clear difference with linear heating in an oven with exposure to an atmospheric environment.

Two aspects have to be considered when designing a laboratory simulation of the thermal shock damage to concrete present in factories: the regime of heating and cooling; and the composition of the spill and concrete. Accordingly, this paper simulates the event of slag spillage in a steel factory. In which, a small amount of molten slag is poured over CAC cement samples at a similar temperature it would have during steel production. This is a novel process that allows a better comparison of the thermo-chemical and thermo-physical effects on the material due to the small scale and controlled environment of the experiment.

The main aim of the authors is to identify different processes taking place on samples with different saturation conditions and water to cement (W/C) ratios. To avoid further changes in the microstructure of the samples after the thermal shock, these had their hydration stopped by means of epoxy impregnation or solvent exchange right after the experiment. A finite element model was used to estimate differences in temperature gradients caused by changes in material design. Finally, a combination of electron microscopy, energy dispersive spectroscopy, thermal gravimetric analysis and X-ray diffraction was used to investigate the microstructure and chemistry of the samples. Assumptions regarding durability and cost effectiveness can be drawn from the presented observations.

2. Materials and methods

2.1. Samples and exposure

Four cylindrical cement paste samples were cast in a plastic mould with the dimensions of $\varnothing$ 55 × 25 mm. Because the focus is on the interaction of molten slag with the binder phase, it was chosen to use cement samples, rather than mortar or concrete samples. The cement used was calcium aluminate cement Calight 50 N. Normal tap water was used for the mix. Two of the samples had a W/C ratio of 0.4 and the remaining two had a W/C ratio equivalent to 0.2. To improve fluidity, MasterGlenium 51 was added as superplasticizer to the samples with the lowest W/C ratio, the quantity added was 0.4% with respect to the cement mass. The samples required no vibration. As CAC hardens considerably faster than Portland cement, only seven days are required to achieve a relatively stable microstructure with most of the hydration finished [15]. Therefore, curing a CAC mixture beyond 7 days should not have any added value. After 24 h, the specimens were de-

moulded and moved to a curing room to remain at 95% humidity and 20 °C temperature for seven days.

One sample of each W/C ratio was submersed in water for 24 h and then was exposed to molten slag. Finally, one sample of each W/C ratio was dried for 48 h at 40 °C in an oven prior to exposure to molten slag. The samples saturated with water are herein called S2 and S4, while the samples dried in the oven are called D2 and D4. The numbers are representative of the W/C ratio, while the letters are representative of the state of the sample during the pour of slag (see Fig. 1, top left).

The slag used for pouring on top of the samples was blast furnace slag, the composition of the slag and the cement used can be found in Table 1. Prior to pouring, 60 grams of slag was heated at 15 °C/m until 1530 °C in an alumina crucible. After 30 min at this temperature, the oven was opened and the crucible was removed and tilted on the samples to pour liquid slag. To keep the slag on the surface of the samples and avoid leakage to the sides, a titanium ring with an inner diameter of 55 mm and height of 35 mm was placed around each sample. Sample and ring were placed on top of a refractory magnesia brick for safe operation. Fig. 1 (top right) shows a sketch of this procedure.

2.2. Temperature estimation

For the estimation of the temperature gradients in each sample, COMSOL® 5.3, a finite element software was used. Solid Mechanics and Heat transfer in Porous Media bundles of COMSOL® 5.3 were used and coupled through thermal expansion multi-physics. A geometry was created to mirror each sample lying on top of a Mg refractory brick with molten slag on top of it contained by the used titanium rings. The thickness of the slag corresponded to the thickness observed post cooling. A triangular mesh was used with adaptive refinement during all calculations. The time steps were taken in logarithmic scales to range from 0.0001 min to 100 min, when cooling was nearly complete. Because the simulation requires several properties as input, these were provided based on an earlier experiment, in which an identical material was subjected to similar conditions and a thermal probe was used to calibrate the inputs. Details of this experiment can be found in a previous study by the authors [16]. Further, the temperature estimation was later used to simulate the stress and strain in each sample. In order to improve the computation time, only one quarter of the samples was used for the mechanical simulations and symmetry was imposed in both cut faces.

The simulations considered the water content and different W/C ratios of the samples as differences in relative humidity of the pore network, vapour permeability and porosity of the material. The slag was modelled as a poured liquid that changes phase during cooling. The transition from liquid to solid was modelled at 1350 °C with a transition interval of 80 °C and latent heat of transition equivalent to 294 kJ/kg in accordance to Kashiwaya (2010) [19].

2.3. Powder analysis

After being exposed to molten slag, the samples remained cooling for 12 h at 20 °C and then the vitrified slag was removed and the specimens were cut in half. From one half, material was extracted from the very top (which was in contact with slag) and gently ground with an agate mortar in preparation for XRD. Prior to grinding, the material was dried through solvent exchange. Approximately 5 grams of powder from each sample was collected and kept dry until testing. Sufficient material was collected for thermogravimetric analysis (TGA) as well, these samples were designated as D2T, S2T, D4T and S4T. The same procedure was repeated for the bottom of each sample, where temperatures
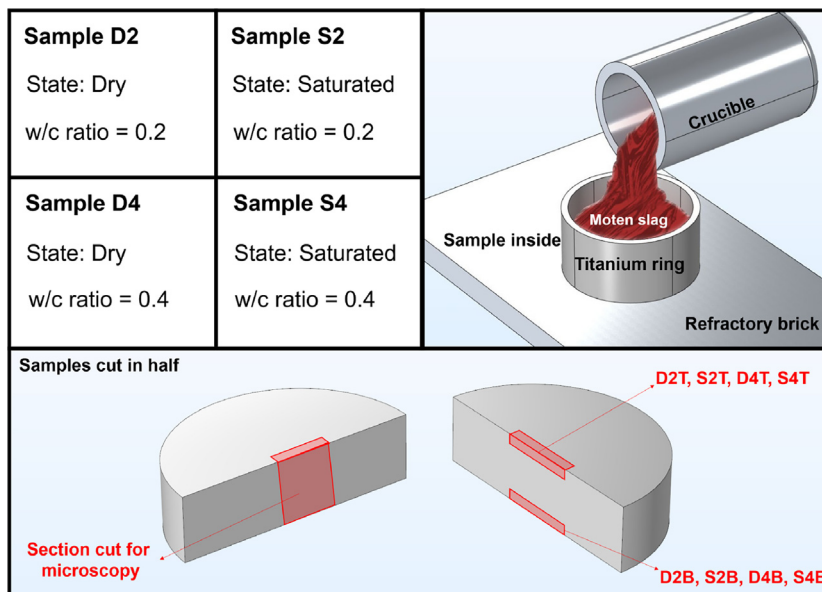
F.F. Mendonça Filho, C. Romero Rodriguez, E. Schlangen et al.

Materials & Design 217 (2022) 110623

Fig. 1. Top left: Naming convention of samples. Top right: Sketch of thermal shock experiment. Bottom: Location of analysed parts in each sample.

Table 1
Chemical composition of materials as determined by XRF.

	SiO_2	Al_2O_3	CaO	MgO	Fe_2O_3	SO_3	Na_2O	K_2O	TiO_2	P_2O_5	L.O.I.	Total
Calight 50 N	8.01	46.85	38.12	0.55	3.16	0.38	0.07	0.19	2.22	0.17	0.28	100.00
BF slag	34.40	11.53	39.17	7.81	1.42	1.6	0.23	0.58	-	-	1.15	97.89

remained considerably lower during exposure to molten slag. Such samples were designated as D2B, S2B, D4B and S4B (see Fig. 1, bottom).

A Bruker D8 Advance diffractometer Bragg–Brentano geometry and Lynxeye position sensitive detector was used with $CuK\alpha_{1,2}(\lambda = 0.15408nm)$ radiation for all XRD measurements. The scatter screen height was set at 5 mm height, divergence slit V12. The used voltage was 45 kV with a current of 40 mA. The spin was of the sample. All scans were performed with a 2θ angle between 10 ° and 130 °, and a step size of 0.03 °. The counting time per step was of two seconds. A combination of two software, X'Pert HighScore Plus and Jade6 was used for the spectral analysis. The standard software databases sufficed for the identification of peaks.

For the thermogravimetric analysis, a NIETZSCH STA 449 F3 Jupiter was used. Approximately 40 mg of material were used for each analysis. The mass change of samples was continuously monitored while the temperature was raised at a 10 °C/min rate from 40 °C to 1000 °C. In order to perform the measurements, a 1 mm^3 alumina crucible containing each sample was placed under a dry argon atmosphere with a purge rate of 50 mL/min.

2.4. Microscopy

The other half of each sample was cut into 25 × 25 × 10 mm to allow a surface containing both, top and bottom of the original cylinders. Each specimen was then vacuum impregnated with epoxy resin. The impregnated specimen surfaces were ground using SiC grinding papers with increasing mesh number from #320 up to #1200. Next diamond pastes of 9 μm, 3 μm, 1 μm and 1/4 μm were used for polishing until a scratch-free surface was achieved in SEM-BSE imaging at about x1000 magnification. Between each grinding and polishing step, the samples faces were

washed with ethanol, then small particles were detached using ultrasonic bath for 1 min and finally the surface was gently dried using compressed air.

The polished sections were analyzed using BSE (backscattered electron) imaging and energy dispersive X-ray spectroscopy (EDS). The microscope used was a QUANTA™ FEG 650 from Thermo Scientific™ equipped with a field emission gun and circular backscatter detector. The samples were analysed under high vacuum, with a take-off angle of 34.6 ° and sample to detector distance of 10 mm. The detector was a SUTW (sapphire) with a calibrated resolution of 132 eV, the accelerating voltage was set at 15 kV for all EDS measurements and the deadtime remained at approximately 10%. The beam current was constantly measured through a picoammeter. The interaction volume of all phases was modeled using CASINO_v2 and all volumes were estimated between 3 and 6 microns for the mentioned accelerating voltage. At times, several SEM images were stitched for a better field of view of the samples, all stitching was performed digitally using the algorithm proposed by Preibisch et at (2009) in [17]. The presented atomic ratios are the average of tens of points taken at hydration products on the same section of a sample.

3. Results

3.1. Temperature simulation

The goal of the FE simulations was to estimate the temperature distribution in the samples during the pouring of slag. Because of the small size of the specimens, the use of multiple thermocouples presented many practical difficulties. Fig. 2 shows the evolution of temperature at the top (at a point 500 μm beneath the surface) and at the bottom (at a point 500 μm above the interface with the MgO brick) of each sample.
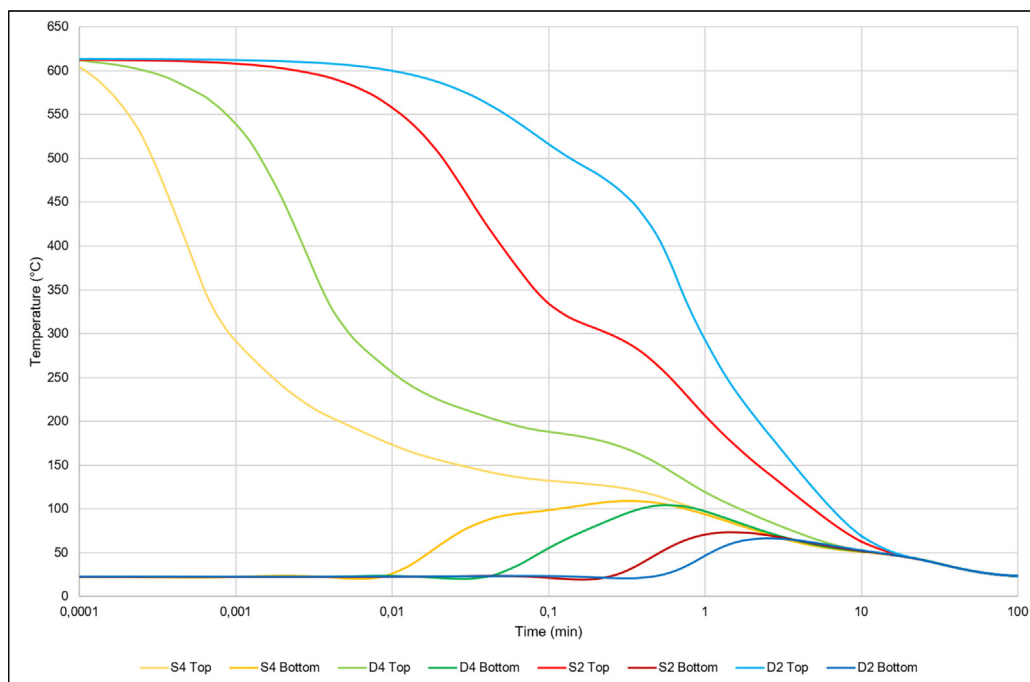
Fig. 2. Estimation of temperatures at specific points in each sample.

While the slag is poured at a temperature close to 1500 °C, a large amount of heat is quickly dissipated due to the escape of water in the same direction of contact with the spillage. Radial contact with the titanium ring and general emissivity of slag at high temperatures also contribute for initial loss of heat. The results show that the maximum temperature does not vary considerably between the top of samples, but rater the duration which this temperature is sustained. Denser samples absorb more heat from the slag, which was observed looking at samples D2 and S2, that remain at high temperatures for longer. Because samples with higher W/C ratio possess more capillary pores, there is more water and air to act as thermal insulation, which would delay the heat transfer from the molten material to the samples. Such delay occurs in combination with the faster cooling of slag, which explains the shorter time for which the top region of the samples remain at maximum temperature. Conversely, air is more insulating than water and the saturated samples remain at high temperatures for shorter time. This is because upon contact with the slag, saturated samples quickly release most of the water, causing the molten pour to bubble during the first seconds, while the dry samples simply start absorbing the heat upon contact with the slag.

Yet, the absorbed heat seems to be more readily dissipated by the samples with lower W/C ratio, as can be inferred by the steeper slope of the Temperature vs time curves of S2T and D2T. This should also be explained by the lower amount of air acting as insulation. The described effect can be observed by the trends in the temperature evolution at the bottom, which shows samples with W/C ratio of 0.4 reaching more than 100 °C, while the remaining specimen have a maximum of 70 °C.

3.2. Thermogravimetric analysis

The thermal gravimetric analysis showed the presence of three zones of interest for all 8 samples, albeit at different magnitudes (Fig. 3). The first zone is located between 100 °C and 200 °C; the second zone is adjacent to the first, between 200 °C and 350 °C; and the last zone of interest is between 700 °C and 800 °C degrees. Table 2 shows the loss due to slag spillage at the top of the sam-

ples, with respect to the values measured at the bottom of each respective sample in correspondence of the observed peaks.

The peaks at the first zone are likely a convolution of the decomposition of two phases, CAH_{10} (usually with wide peaks around 125 °C [18]) and C_2AH_8 (usually with wide peaks around 190 °C [5]). These two phases are the hydration products with most attached water molecules found in CAC, and the first ones to decompose. All but one sample show a significant decrease in mass loss correspondence between the peaks of the top and the bottom region of the samples. Which points to dehydration of the mentioned phases during the spillage experiment. Sample S4 is the exception, these phases seem to have remained relatively at the same ratio for top and bottom. This is possibly due to the temperature at the bottom reaching the dehydration temperature of CAH_{10}. Furthermore, the peaks from the bottom part in samples D4 and S4 were skewed towards 200 °C, while the peaks for the top part were not. Because this is only seen in samples D4 and S4, it is likely caused by the imperfect dehydration of CAH_{10} (following Eq. 1 [21]) during the contact with molten slag.

$$2CAH_{10} \rightarrow C_2AH_8 + AH_3 + 9H \tag{1}$$

Which results in the increase of the amount of C_2AH_8. As sample S2 is presumed to have reached slightly higher temperatures than sample D2 at their respective bottoms (on Fig. 2), it is also noticeable on the DTG results that sample S2 has a slight skew toward the same side as samples D4 and S4.

Correspondingly, the peaks in the second zone of interest are also likely to be the combination of two decomposed phases. Namely, AH_3 shows dehydration around 260 °C [5] and C_3AH_6 between 280–310 °C [18]. This is somewhat expected, since the dehydration of C_2AH_8 generates C_3AH_6 and AH_3 (Eq. 2 [7]).

$$3C_2AH_8 \rightarrow 2C_3AH_6 + AH_3 + 9H \tag{2}$$

As the temperatures at the bottom of the samples were unlikely to have reached values close to the dehydration of the two mentioned products, samples D2, S2 and D4 show a clear difference with respect to the curves obtained from material at the top of the samples.
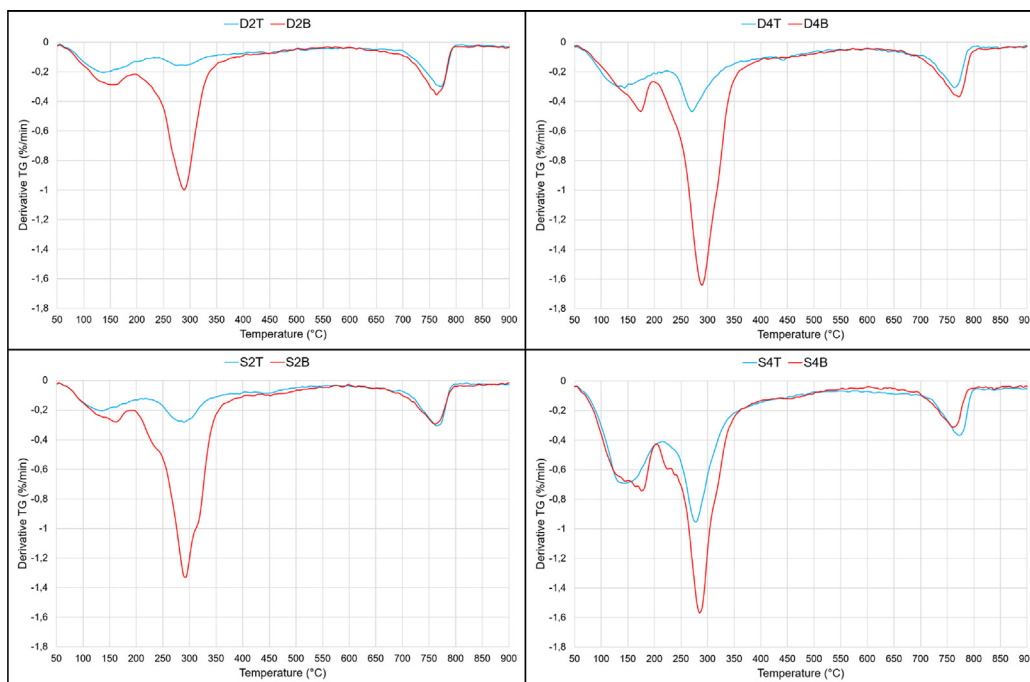
F.F. Mendonça Filho, C. Romero Rodriguez, E. Schlangen et al.

Materials & Design 217 (2022) 110623

Fig. 3. Derivative thermogravimetric analysis of samples comparing top and bottom composition.

Table 2
Decrease in peak minimum between powder collected from the top and from the bottom of each sample.

Sample	Peak 1	Peak 2	Peak 3
D2	29%	84%	16%
S2	27%	79%	−3%
D4	34%	71%	17%
S4	7%	39%	−18%

Table 3
Chemically bound water for top and bottom samples as calculated from TGA analyses.

Samples	Chemically bound water (%)
D2T	7.3
D2B	14.4
S2T	8.4
S2B	17.3
D4T	11.1
D4B	21.2
S4T	19.4
S4B	22.8

Comparing only the curves for the top of the samples, it is apparent that sample with W/C ratio of 0.4 present a greater mass loss. This is likely due the higher amount of water during hydration, which allows for the formation of more CAH_{10} and eventually its conversion to C_3AH_6. This also holds when comparing the dry samples to their respective saturated pairs. Thus, the greatest peak between 100 °C and 200 °C in sample S4T is accompanied by the greatest peak between 200 °C and 350 °C in the same sample.

In calcium aluminate cement, the dehydration peak between 700 °C and 800 °C is believed in literature [20] to be due to the conversion of $C_3AH_{1.5}$ to mayenite. As the temperatures in the samples are predicted to not have surpassed 700 °C, the difference between curves from the bottom of the samples and from the top is small. However, the formation of the intermediary phase $C_3AH_{1.5}$ is believed to usually happen in relatively high pressure environments [22]. As all samples presented the peak, it is believed that all specimens suffered from high capillary pressure due rapid vapour expansion during contact with the molten material. Furthermore, the dry samples present greater mass loss in correspondence with the peaks in the curves respective to their bottoms, implying lower pressure at the top, possibly due to cracking or fast water escape. On the other hand, the peaks magnitudes for both saturated samples were higher on the top than the bottom. This is likely due the higher amount of water present in the sample and its route of escape, causing a higher pore pressure environment.

The total loss of chemically bound water is displayed in Table 3. The TGA results were in good agreement with the FE simulations,

validating the initial assumption of fast cooling of slag from 1500 °C to 600 °C.

3.3. X-ray diffraction

The results of XRD for samples with W/C ratio of 0.2 are presented in Fig. 4 and the remaining samples in Fig. 5. As expected, the peaks corresponding to unhydrated particles remain constant, with CA as the main phase and CA_2 and CA_4 in smaller amounts. Although CA_4 is not as common in CAC as the two other phases, it can be often found in higher purity cements [23].

Next, gibbsite is present in all bottom spectra, but absent on all spectra from the top of the samples. In addition, most hydrogarnet peaks are strongly decreased between top and bottom scans, with the exception of sample S4. Calcium aluminate decahydrate peaks were absent in all samples but S4, presumably because of the small quantity and background noise. Alternatively, CAH_{10} can lose crystalinity through partial conversion, this is a solid state decomposition in which the phase will slowly (at the studied temperatures) convert to C_2AH_8 [24]. The characteristic peak for C_2AH_8 falls outside of the range studied. These results present a strong correlation with the thermogravimetric analysis, including the stronger remaining peaks of CAH_{10} on sample S4, as it will be discussed later.
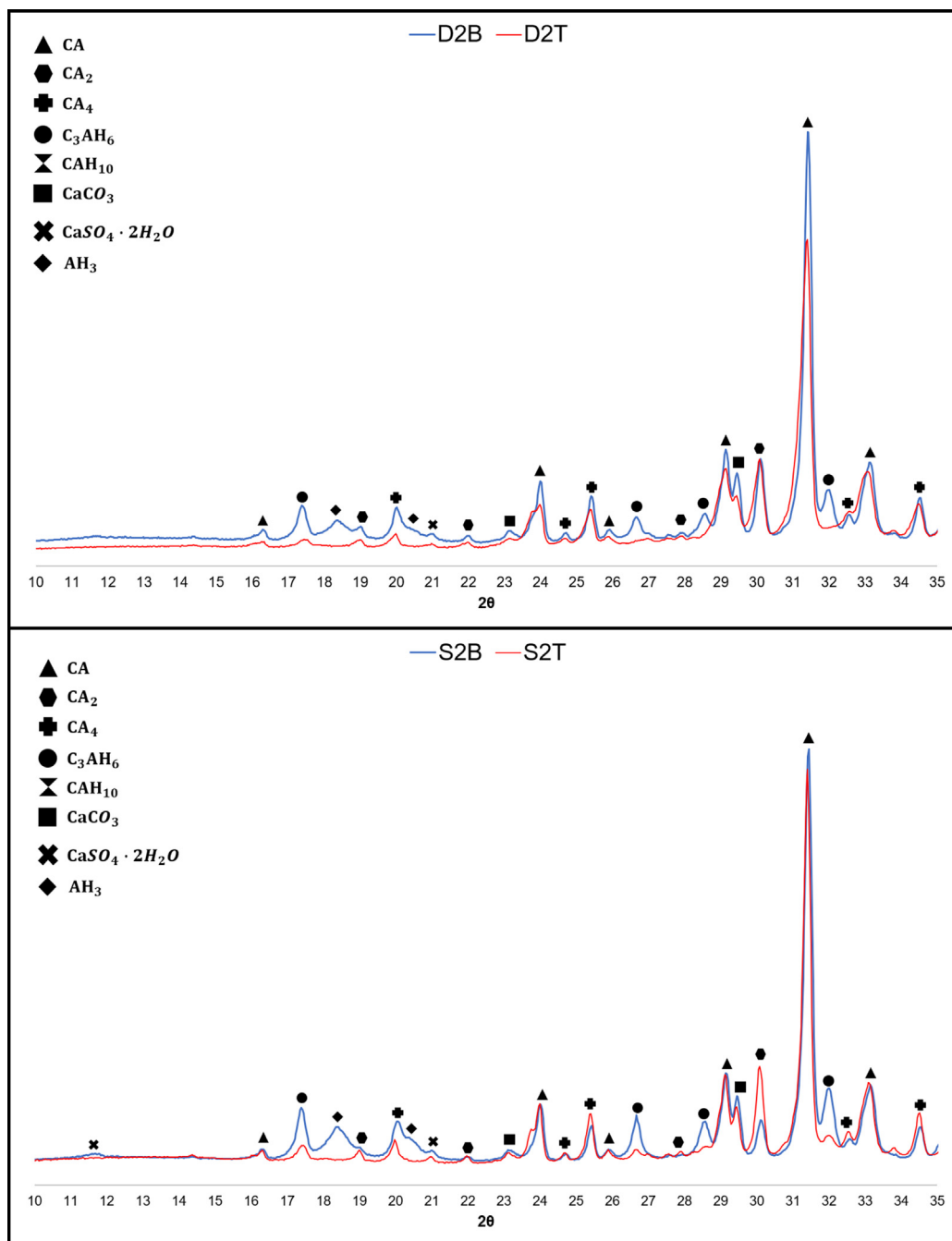
F.F. Mendonça Filho, C. Romero Rodriguez, E. Schlangen et al.

Materials & Design 217 (2022) 110623

Fig. 4. X-ray diffraction results for samples comparing top and bottom composition.

Gypsum has an overlapping decomposition temperature with CAH_{10}, thus can be easily missed in the DTG results. However, trace quantities were found in the XRD spectra. These are notably present in samples S2B and D4B, albeit absent in samples S2T and D4T. Which is to be expected due the comparatively easy dehydration of this phase. Likewise, trace amounts of calcite were also detected.

3.4. Electron microscopy

Sample D2

This sample presented a dramatic change in phases characteristic size from top to the bulk of the sample. This effect was visible only in the first millimetres of the surface, becoming homogeneous after 2 mm. Fig. 6 shows this disparity.

The top of Fig. 6a) corresponds to the face of the sample onto which molten slag was poured. This effect is present over the entire width of the sample. Within the first 500 μm from the top, the phases are mostly between 0.5 μm and 2 μm in diameter and never above 5 μm. Between 500 μm deep and 1 mm, the phases become bigger, with unhydrated particles between 5 μm and 20 μm. After a millimetre the sample starts to present average particle sizes similar to its bulk, with some unhydrated particles bigger than 50 μm. Besides the difference in particle sizes, bright grey phases occur at the top right of Fig. 6a) and 6b). Finally, there is a clear decrease in unhydrated grains size and occurrence from
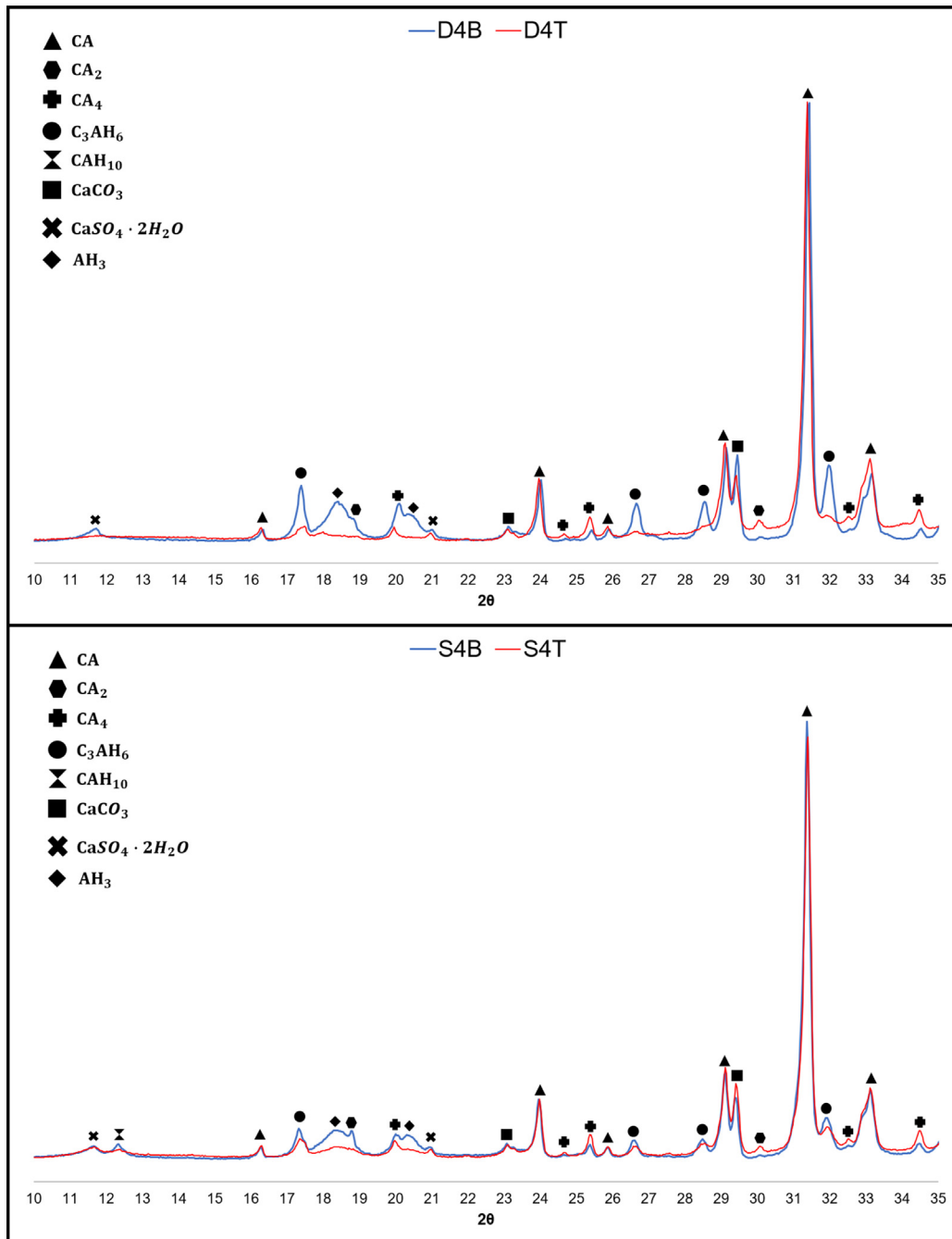
Fig. 5. X-ray diffraction results for samples comparing top and bottom composition.

the first 1000 µm of the sample. This specimen displayed a comparatively simpler chemistry than the others.

Analysing the composition of the sample, The EDS spectra taken from the bright phases consistently displayed higher Ca/Al and Si/Al ratios than in any other zones of the sample. Further, siliceous hydrogarnet's (C_3ASH_6) approximate density is of 2.83 g/cm^3 [26], while CAH_{10}, C_2AH_8 and C_3AH_6 densities are 1.74 g/cm^3 [25], 1.95 g/cm^3 [26] and 2.53 g/cm^3 [26], respectively. Thus, the bright gray value phases are likely siliceous hydrogarnet.

Sample S2

This sample presents no signs of the chemical changes observed on the previous one. Rather, the major effects seem to have been physical, in the form of cracks formed parallel to the surface exposed to slag spillage (see Fig. 7, left). This crack pattern was

observed throughout the top three millimetres of the sample on the entire area prepared for SEM.

When compared to the phases in the bottom of the sample, the top of the sample seems to have few differences. The average atomic composition remained similar independent of depth. Although, some needle like structures were observed exclusively in this sample, as seen in Fig. 7, right. The needles in the top right of the figure display the same gray values and EDS spectra than CAH_{10}, which might indicate re-hydration took place during the cooling of the sample. On the bottom right of the figure, the needles also present similar composition, with the distinction of high amounts of potassium. Indeed, in certain spectra, the atomic amount of K surpassed Ca. This could be a sign of replacement of calcium to form alkaline aluminate hydrates as it is known to
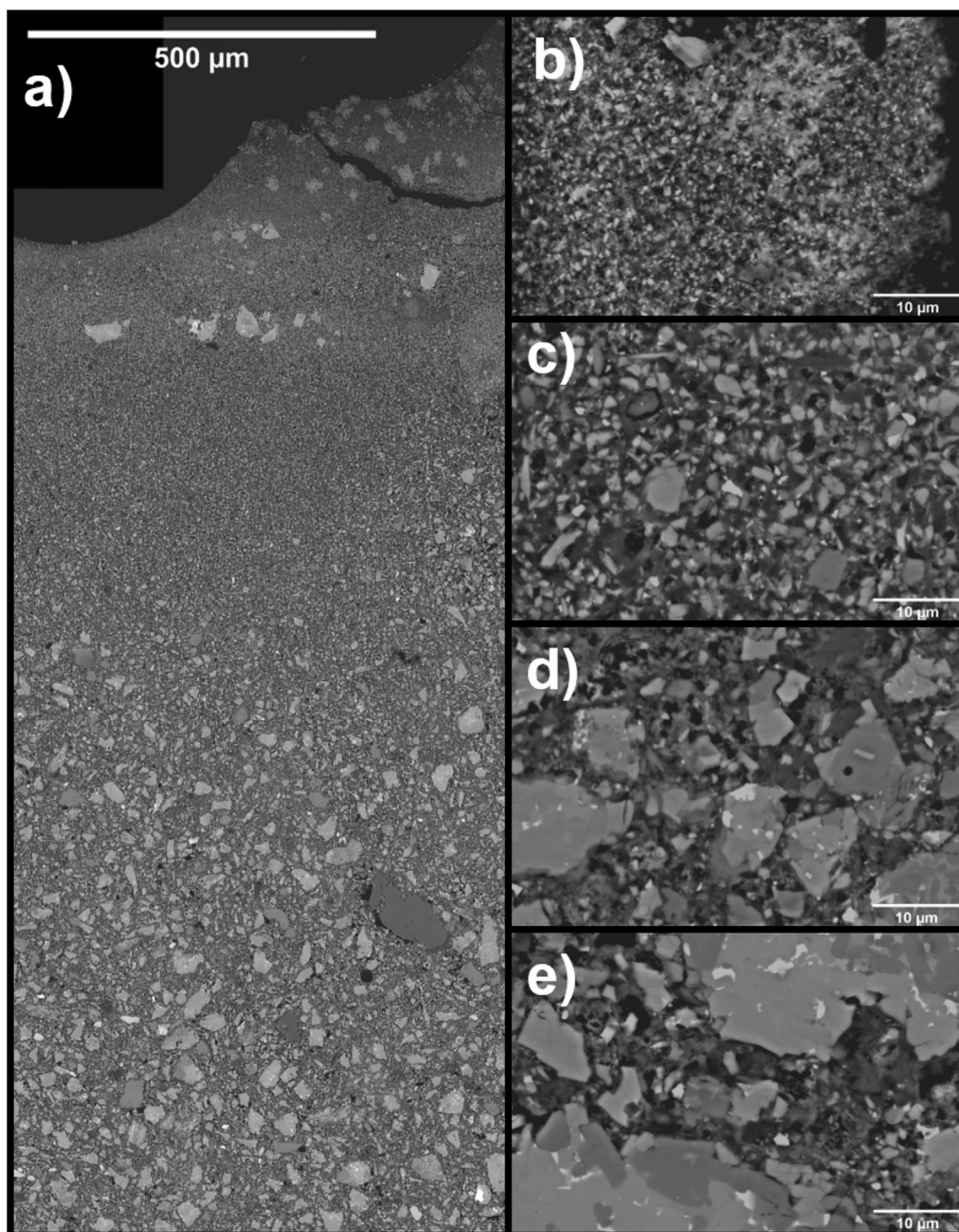
F.F. Mendonça Filho, C. Romero Rodriguez, E. Schlangen et al.

Materials & Design 217 (2022) 110623

Fig. 6. Sample D2; a) Sample overview composed of stitched micrographs; b) SEM image of particles size at the very top of the sample; c) SEM image at 400 μm from the surface; d) SEM image ate 800 μm from the surface; e) SEM image at 1500 μm from the surface.

precipitate at higher pH through the reaction in Eq. 3 [28]. However, as this was rarely found in the sample and the characteristic peaks were absent in XRD analysis, hence a minor effect.
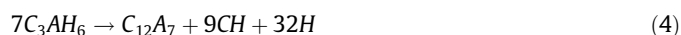
$$CAH_{10} + 2KH \leftrightarrow CH + KAH_6 + 4H \qquad (3)$$
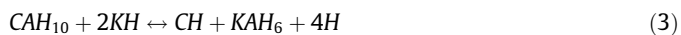
Sample D4

A sample overview at different scales is shown in Fig. 8. There was considerably less cracking in this sample in comparison with the previous one. Further, most cracks were perpendicular to the surface and extended only through the first millimetre of the top.

Along the entire surface of the sample there was a layer of 5 μm to 30 μm of a dark phase with an intricate microcracks pattern. This can be observed in Fig. 8 center and right. The composition of this phase is consistent with gibbsite, however, its low grayscale value points to AH_3 gel rather than its crystalline correspon-

dent. Because this phase is seen predominantly at the top of the sample, it is likely that it is not a product of hydration or conversion, but of the decomposition of the main components of the cement, which also produce AH_3 (see Eqs. 1 and 2).

Beneath this layer, the composition of the main binding phases seems similar to CAH_{10} and C_2AH_8, however, partially dehydrated. This is observed by the proportional difference in oxygen detection and higher amount of voids in comparison with the bulk of the sample. The phases with brighter gray values than AH_3 and CAH_{10}, but darker than the unhydrated particles, are very rich in calcium and present few of the other elements. This could possibly be explained by the dehydration of C_3AH_6 forming portlandite, as in Eq. 4 [27].
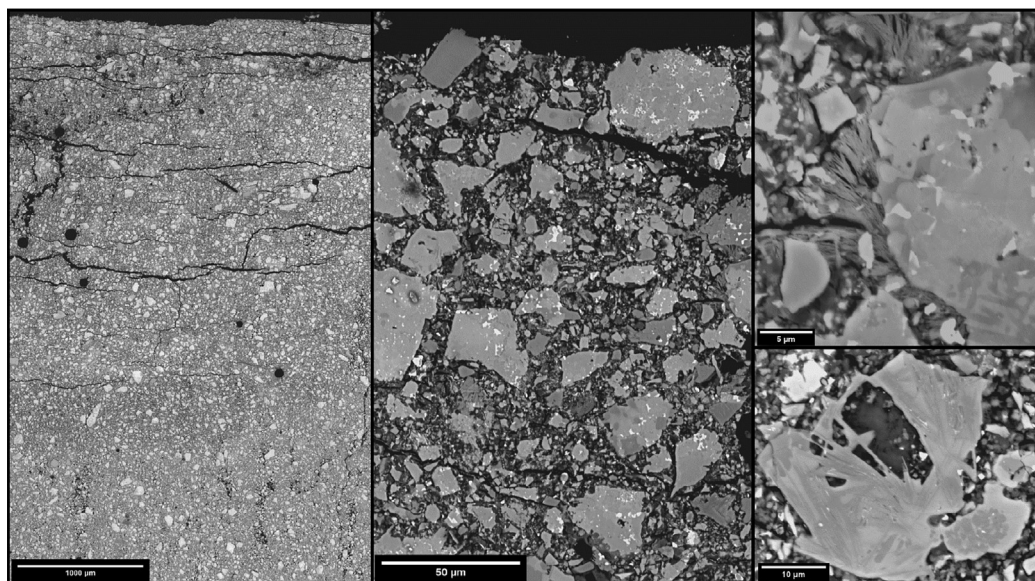
$$7C_3AH_6 \rightarrow C_{12}A_7 + 9CH + 32H \qquad (4)$$

F.F. Mendonça Filho, C. Romero Rodriguez, E. Schlangen et al.

Materials & Design 217 (2022) 110623

Fig. 7. Sample S2; Left: overview of sample and surface cracking; Center: display of sample main phases; Right: needle-like structures.
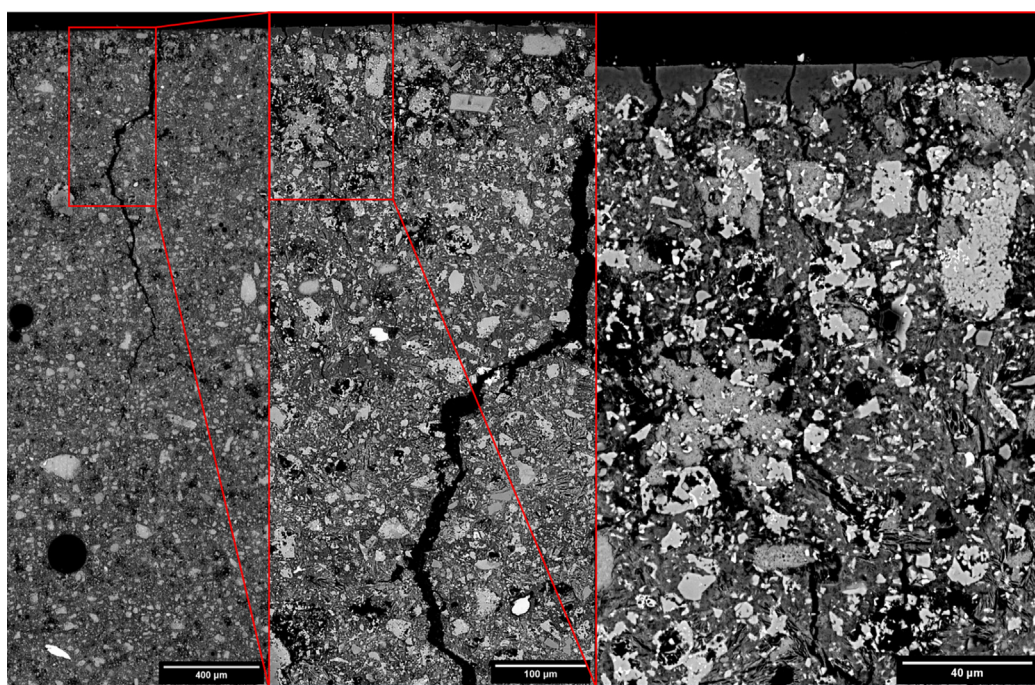

Fig. 8. Sample D4; Left: Sample overview composed of stitched micrographs; Center: Zoomed in image of the red square present in left image; Right: Zoomed in image of the red square present in center image.

Although the change in size and occurrence of unhydrated grains is not noticeable in this sample, an increase in voids around such grains was detected, which further supports this hypothesis. The remaining unhydrated grains demonstrated a very high concentration of Si, which might indicate the dehydration of C_3ASH_6 rather than C_3AH_6.

Sample S4

Finally, an overview of sample's S4 microstructure can be seen in Fig. 9. It did not show significant cracking, despite being the sample with the most water. It also did not showed differences in the unhydrated grains.

As in the last sample, the same consistent 5 μm to 30 μm layer of AH_3 gel is present. The gel is mixed with other phases between unhydrated grains for more 30 μm to 100 μm. Past this layer, there is a well defined porous zone with 90 μm to 230 μm of thickness. The composition of this porous zone, once again, has a much higher Ca/Al atomic ratio than in the rest of the sample. After that, the sample displays very little difference to phase composition and distribution present at the bottom.

Atomic ratios comparison

Besides the localised effects, the bulk chemistry of the hydration products was investigated in the samples taking the average

F.F. Mendonça Filho, C. Romero Rodriguez, E. Schlangen et al.
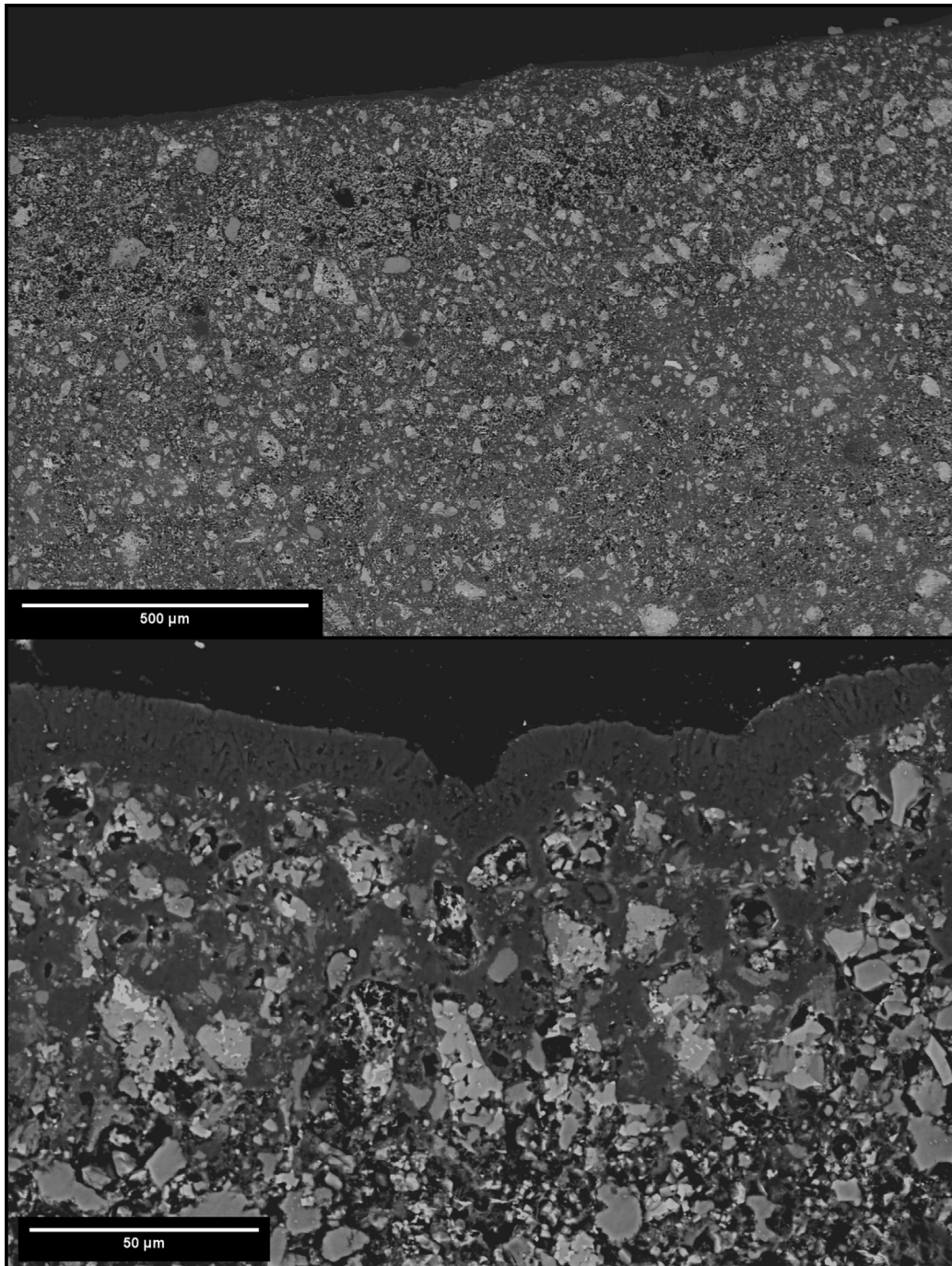
Materials & Design 217 (2022) 110623

Fig. 9. Sample S4; Top: stitched overview of sample surface; Bottom: Zoomed in view of sample surface.
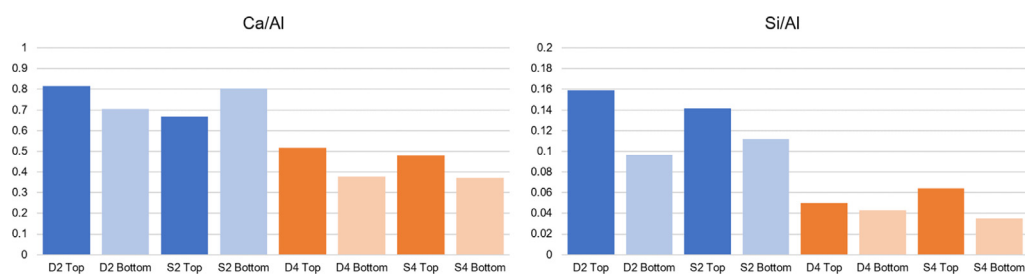
Fig. 10. Atomic ratios of samples as of measured by the average of EDS points.

F.F. Mendonça Filho, C. Romero Rodriguez, E. Schlangen et al.

Materials & Design 217 (2022) 110623

composition of tens of EDS points near the top and near the bottom of each sample. Fig. 10 shows the summarized results for Ca/Al and Si/Al ratios.

Both atomic ratios are higher in samples with lower W/C ratio, independent of pre-treatment to receive slag or the region of the sample being studied. This is likely due the higher amount of AH_3 in the samples with 0.4 of W/C ratio. Greater availability of water during hydration at room temperature can also allow for more production of AH_3 [6]. The higher temperatures estimated for these samples could further force conversion, which produces more AH_3 [32]. Finally, both samples D4 and S4 also had plenty of AH_3 gel in its surface.

Additionally, the Si/Al ratio is always higher at the top of the samples than at the bottom. Looking at Table 1, the cement samples represent an environment saturated in Ca (the main component of the used slag), but undersaturated in Si, the second most abundant element in the molten material. Although literature is scarce for the exact conditions of this experiment, the diffusion of Ca and Si in calcium aluminosilicate slags under ultra high temperatures has been studied [30,31], which is somewhat comparable. Thus, it is possible that silicon diffused to the cement in a first moment, when the slag still had a temperature superior to 1000°C.

4. Discussion

4.1. Thermo-mechanical damage

The biggest physical modifications were observed in samples S2 and D4, in the form of cracking in the face receiving the molten slag. However, these two samples present opposite forms of cracking. Sample S2 displayed horizontal fracture parallel to the plane of heating by the slag, while sample D4 had vertical cracks, orthogonal to the plane being heated. The authors believe that this can be explained by the temperature gradient and consequent strain distribution within the cement paste.

The maximum volumetric strain for both samples occurred between 0.1 and 1 min. Looking at this interval of time in Fig. 2, the temperatures at the top and bottom of sample D4 had less than 100 °C of difference, while sample S2 was mostly heated at the top, with the bottom still at room temperature, causing a gradient of about 300 °C. Fig. 11 shows the simulated strain fields of both 0.2 min after the exposure.

Sample D4 had a well distributed strain field, with the higher temperatures at the top causing typical dilation cracks. Sample S2 had a very sharp difference in strain between the top millimeter and the bottom of the sample given by the poor temperature distribution at that moment in time. Such acute difference can cause shear stresses, contributing to horizontal cracking. However, sample D2 had a similar strain field without displaying cracking. The

authors believe this is the contribution of the moisture state of the samples. While D2 was dry and had only chemically bound water released (at a much higher temperature), sample S2 had a considerable amount of physically bound water evaporating almost instantly after exposure to the molten slag. The vapour expansion caused elevated stresses through the well known thermo-hydral damage mechanism in concrete [10] and the summation of these with the shear stresses caused by the thermal dilation are believed to be responsible for the horizontal cracks. Regarding sample S4, it is clear that the temperature gradient (and ergo the stress and strain fields) were milder, given the physically bound water being able to quickly escape and act as a coolant agent to the molten slag.

4.2. Thermo-chemical alterations

Three phenomena are dependent on the duration of heating during high temperature exposure: transformations in porosity, chemical composition and occurrence of new phases [29]. Sample D2 is estimated to have endured high temperatures at least one order of magnitude longer than all other samples, and accordingly, is the sample with most changes in porosity and composition.

Both, the conversion and dehydration reactions of the main phases generate water molecules (see Eqs. 1, 2 and 4). Therefore, it is possible that the decrease of size and occurrence of unhydrated particles in sample D2 is connected to the presence of C_3ASH_6. Conceivably, dehydration of lower depths of the sample generated water propelled to escape through the top of the sample. Such water would be in the form of vapour at high pressure and high temperature. Its contact with the top portion of the sample could have caused steam curing. This would also agree with the overall decrease in porosity at the topmost layer.

As established in several investigations [7,33–36], CA hydrates to directly form C_3AH_6 above 60 °C. However, C_3ASH_6 is found in opposition to C_3AH_6. This is due the high availability of Si, as commented on the results section. The main reason for such availability could be explained by the indirect dissolution of the slag into the cement acting as refractory. Braulio et al. [37] describes a simpler system of samples also using CAC as a binder, in which the authors have shown that the dissolution of slag within the refractory and the precipitation of different products caused by it. In accordance, Fig. 10 of the present experiment shows that slag predominantly contributed with the increase of Si atoms into the cement, causing an environment idealized in the scheme presented in Fig. 12.

Although it is possible to form CAH_{10} at high temperatures for a short period of time, this depends on the availability of high crystalinity AH_3 [39], which was not found on the XRD results. Further, the TGA results support this conjecture given the almost flat curve of D2T with respect to $CAH_{10}, C_2AH_8, C_3AH_6$ and AH_3.
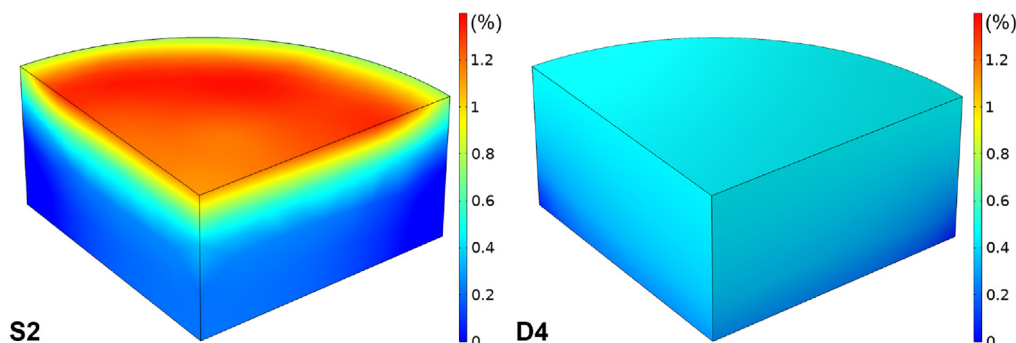

Fig. 11. Simulated volumetric strains (%) for samples S2 and D4 at 0.2 min.

F.F. Mendonça Filho, C. Romero Rodriguez, E. Schlangen et al.
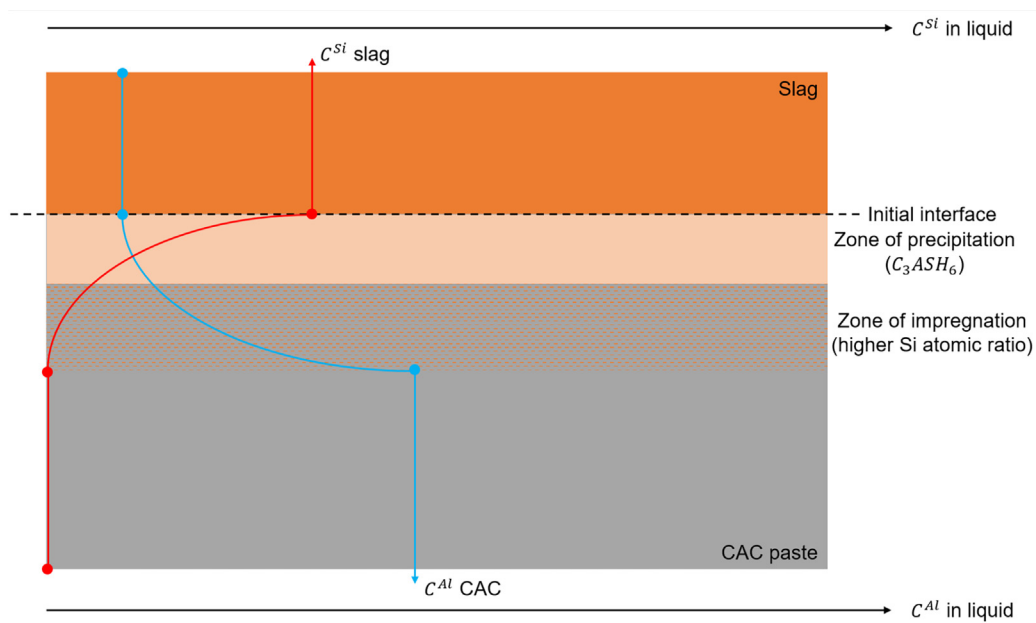
Materials & Design 217 (2022) 110623

Fig. 12. Scheme of the indirect dissolution taking place on the samples during the contact with molten slag (adapted from sketch in Poirier & Rigaud [38]).

Assuming this depicts the processes taking place at sample D2, what would explain the lack of similar products in sample S2, which also endured a relatively longer period of high temperatures? The cracking allows for prompt release of pressure and faster escape route for water, which precludes the conditions necessary for steam curing as hypothesized in the previous sample. In accordance, TGA and XRD peaks are notably larger for sample S2, displaying the presence of remaining C_3AH_6 and possibly CAH_{10}. The lack of chemical complexity found by SEM EDS investigation would further agree.

While samples D2 and S2 can be seen as two extreme cases in terms of either thermo-mechanical or thermo-chemical chemical alterations, sample D4 is somewhat of a middle ground. The thermo-hydral mechanism depends on the amount of water, tensile strength and heating rate [40]. This sample contained less physically bound water than sample S2 and also a lower tensile capacity due its higher W/C ratio [41]. As a result, cracking occurred mildly and chemical changes were less pronounced. However, a zone of amorphous AH_3 was identified at the very top of the sample. The higher porosity zone beneath the top of the sample points to dehydration of phases, which would also provide water availability for upper layers. As cracking was less distributed, this could provide a less severe environment, in which residual water binds with available aluminum ions to generate the upper layer.

Sample S4 displayed the least estimated exposure in time at very high temperatures, quickly reaching ∼150 °C, in agreement with the large peaks for hydration products present in the results of XRD and TGA. Further, as the sample that presented longer bubbling of slag, its direct contact was slightly delayed. This resulted in a structure similar to sample D4 in terms of a upper layer of amorphous AH_3 followed by a porous zone. But, with less evident changes.

However, for the same W/C ratio, sample S4 had more physically bound water, so it should suffer more damage from evaporation. Yet, the sample remained undamaged. The authors believe that the combination of faster cooling of the slag by the water released on this sample and the very short time at temperatures above 200 °C, caused a much smoother heating rate and strain field

in comparison to sample D4. Such decrease, should be enough to avoid damage [42,43].

5. Conclusion

The authors attempted to reproduce an industrial hot spillage event at laboratory scale with controlled variables in order to study its effects on the CAC-based structural material subjected to the spill. As expected, the effects on the microstructure of the material considerably differ from experiments where such materials are subjected to a uniform thermal loading i.e. oven heating.

The main processes apparently taking place on the material during contact with molten slag were:

1. The decomposition of the hydration products;
2. The escape of physically bound water, causing thermo-hydral spalling damage in some of the samples;
3. Possibly the steam curing of the surface in contact with the hot spill for non-cracked and mildly cracked samples;
4. Possible diffusion of Si from the slag into the binder, given enough time of contact at high temperature.

While heating samples can simulate the first effect very well, the other effects are very geometry sensitive and not comparable on different methods. As the other effects show an appreciable influence in the performance of the samples, the authors believe that the novel method proposed herein to be more suited to simulate industrial events.

Furthermore, an attempt to accurately describe the behaviour of the samples was made, observing that a W/C ratio of 0.2 would grant better durability provided the structure is sure to remain dry. If there is a risk of having a saturated structure (i. e. outdoor installation), the counter intuitive strategy of a higher W/C ratio seems to be preferable. This has only be tested to a limit of 0.40 ratio, as it is known that higher W/C values bring different forms of durability problems due adverse effects of conversion [6,7].

Both steam curing and Si diffusion into the material could be beneficial for the structural durability under repeated events. However, supplementary investigations are necessary before con-

firming these effects. This shows the need of cyclic thermal shock experiments for concrete.

Finally, large scale events might also enhance the thermo-mechanical damage of concrete depending on the degrees of freedom of the structural elements. Future research endeavours could possibly create setups in which samples have strain restrictions to take this effect into account.

Declaration of Competing Interest

The authors declare that they have no known competing financial interests or personal relationships that could have appeared to influence the work reported in this paper.

Acknowledgements

References

[1] P.K. Mehta, P.J.M. Monteiro, Concrete: Microstructure, Properties, and Materials, McGraw-Hill Education, Berkeley, 2006. ISBN: 9780071462891.

[2] C.A. Britez, C.N. Costa, Ações do Fogo nas Estruturas de Concreto, in: G.C. Isaia (Ed.), Concreto: Ciência e Tecnologia, 1st ed., vol. 2, 2011, pp. 1029–1068. IBRACON (in Portuguese).

[3] Eurocode 2: Design of concrete structures - Part 1-2: General Rules - Structural fire design; German version EN 1992-1-2:2004 + AC:2008.

[4] S.A. Memon, S.F.A. Shah, R.A. Khushnood, W.L. Baloch, Durability of sustainable concrete subjected to elevated temperature - A review, Constr. Build. Mater. 199 (2019) 435–455, https://doi.org/10.1016/j.conbuildmat.2018.12.040.

[5] N.K. Lee, K.T. Koh, S.H. Park, G.S. Ryu, Microstructural investigation of calcium aluminate cement-based ultra-high performance concrete (UHPC) exposed to high temperatures, Cem. Concr. Res. 102 (August) (2017) 109–118, https://doi.org/10.1016/j.cemconres.2017.09.004.

[6] J. Ideker, H., Scrivener, K., L., H. Fryda, B. Touzo, Calcium Aluminate Cements, in: Hewlett, P., C., Liska, M. (Eds.), Lea's Chemistry of Cement and Concrete, 5th ed., Butterworth-Heinemann, 2019, pp. 537–584.

[7] J. Bensted, Calcium aluminate cements, in J. Bensted, P. Barnes (Eds.), Structure and performance of cements, 2nd ed., Spon Press, 2002, pp. 114–139.

[8] E. Nonnet, N. Lequeux, P. Boch, Elastic properties of high alumina cement castables from room temperature to 1600°C, J. Eur. Ceram. Soc. 19 (8) (1999) 1575–1583, https://doi.org/10.1016/s0955-2219(98)00255-6.

[9] Y. Wang, X. Li, B. Zhu, P. Chen, Microstructure evolution during the heating process and its effect on the elastic properties of CAC-bonded alumina castables, Ceram. Int. 42 (9) (2016) 11355–11362, https://doi.org/10.1016/j.ceramint.2016.04.058.

[10] P. Kalifa, F.D. Menneteau, D. Quenard, Spalling and pore pressure in HPC at high temperatures, Cem. Concr. Res. 30 (12) (2000) 1915–1927, https://doi.org/10.1016/S0008-8846(00)00384-7.

[11] A. Ferna, New Cementitious Materials Based on Alkali-Activated Fly Ash:, J. Am. Ceramic Soc. 3314 (2008) 3308–3314, https://doi.org/10.1111/j.1551-2916.2008.02625.x.

[12] G. Debicki, R. Haniche, F. Delhomme, An experimental method for assessing the spalling sensitivity of concrete mixture submitted to high temperature, Cement Concr. Compos. 34 (8) (2012) 958–963, https://doi.org/10.1016/j.cemconcomp.2012.04.002.

[13] I. Hager, T. Tracz, M. Choińska, K. Mróz, Effect of cement type on the mechanical behavior and permeability of concrete subjected to high temperatures, Materials 12 (18) (2019), https://doi.org/10.3390/ma12183021.

[14] F. Aslani, L. Wang, Fabrication and characterization of an engineered cementitious composite with enhanced fire resistance performance, J. Clean. Prod. 221 (2019) 202–214, https://doi.org/10.1016/j.jclepro.2019.02.241.

[15] H.F.W. Taylor, Cement Chemistry, 2nd ed., Thomas Telford Publishing, London, 1997, ISBN:0727725920.

[16] F.F. Mendonça Filho, O. Copuroglu, Re-curing of calcium aluminate cements post contact with molten slag, in: 17th Euroseminar on Microscopy Applied to Building Materials, vol. 50, 2019, pp. 236–24. Retrieved from http://civmin.utoronto.ca/wp-content/uploads/2019/05/35.pdf.

[17] S. Preibisch, S. Saalfeld, P. Tomancak, Globally optimal stitching of tiled 3D microscopic image acquisitions, Bioinformatics (Oxford, England) 25 (11) (2009) 1463–1465, https://doi.org/10.1093/bioinformatics/btp184.

[18] K. Scrivener, R. Snellings, B. Lothenbach (Eds.), A Practical Guide to Microstructural Analysis of Cementitious Materials. CRC Press, Boca Raton, 2016, https://doi.org/10.1201/b19074.

[19] Y. Kashiwaya, T. Akiyama, Y. In-Nami, Latent heat of amorphous slags and their utilization as a high temperature PCM, ISIJ Int. 50 (9) (2010) 1259–1264, https://doi.org/10.2355/isijinternational.50.1259.

[20] C. Phrompet, C. Sriwong, S. Maensiri, P. Chindaprasirt, C. Ruttanapun, Optical and dielectric properties of nano-sized tricalcium aluminate hexahydrate (C3AH6) cement, Constr. Build. Mater. 179 (2018) 57–65, https://doi.org/10.1016/j.conbuildmat.2018.05.180.

[21] V. Antonovi, J. Keriene, R. Boris, M. Alekneviius, The Effect of Temperature on the Formation of the Hydrated Calcium Aluminate Cement Structure, Procedia Eng. 57 (2013) 99–106, https://doi.org/10.1016/j.proeng.2013.04.015.

[22] M.T. Palou, Ľ. Bageľ, V. Zivica, M. Kuliffayova, T. Ifka, Hydration of high alumina cement-silica fume composite with addition of Portland cement or sodium polyphosphate under hydrothermal treatment, J. Therm. Anal. Calorim. 113 (2013) 385–394, https://doi.org/10.1007/s10973-013-3042-2.

[23] D. Fernández-González, J. Prazuch, I. Ruiz-Bustinza, C. González-Gasca, J. Piñuela-Noval, L.F. Verdeja, Solar synthesis of calcium aluminates, Sol. Energy 171 (January) (2018) 658–666, https://doi.org/10.1016/j.solener.2018.07.012.

[24] G. Geng, J. Li, Y. Yu, D.A. Shapiro, D.A.L. Kilcoyne, P.J.M. Monteiro, Nanometer-Resolved Spectroscopic Study Reveals the Conversion Mechanism of CaO·Al2O3·10H2O to 2CaO·Al2O3·8H2O and 3CaO·Al2O3·6H2O at an Elevated Temperature, Crystal Growth Des. 17 (1) (2017) 4246–4253, https://doi.org/10.1021/acs.cgd.7b00553.

[25] P. Villars, K. Cenzual, CAH10 (CaAl2[OH]8[H2O]5.4) Crystal Structure: Datasheet from "PAULING FILE Multinaries Edition – 2012". SpringerMaterials. Springer-Verlag, Berlin Heidelberg & Material Phases Data System (MPDS), Switzerland & National Institute for Materials Science (NIMS), Japan, 2012, https://materials.springer.com/isp/crystallographic/docs/s_1811685.

[26] M. Balonis, F.P. Glasser, The density of cement phases, Cem. Concr. Res. 39 (9) (2009) 733–739, https://doi.org/10.1016/j.cemconres.2009.06.005.

[27] F. Wang, P. Chen, X. Li, B. Zhu, Effect of Colloidal Silica on the Hydration Behavior of Calcium Aluminate Cement, Materials (Basel, Switzerland) 11 (10) (2018) 1849, https://doi.org/10.3390/ma11101849.

[28] S. Goñi, C. Andrade, J. Sagrera, M. Hernández, C. Alonso, A new insight on alkaline hydrolysis of calcium aluminate cement concrete: Part I. Fundamentals, J. Mater. Res. 11 (7) (1996) 1748–1754, https://doi.org/10.1557/JMR.1996.0219.

[29] Z. Ignaszak, P. Popielarski, Contribution to Thermal Properties of Multi-Component Porous Ceramic Materials Used in High-Temperature Processes in the Foundry Industry, in: J.M.P.Q. Delgado (Ed.), Heat and Mass Transfer in Porous Media, 1st ed., Springer, Berlin Heidelberg, 2012, pp. 187–218.

[30] H. Towers, J. Chipman, Diffusion of Calcium and Silicon in a Lime-Alumina-Silica Slag, JOM 9 (1957) 769–773, https://doi.org/10.1007/BF03377932.

[31] K. Zheng, F. Yang, X. Wang, Z. Zhang, Investigation of Self-Diffusion and Structure in Calcium Aluminosilicate Slags by Molecular Dynamics Simulation, Mater. Sci. Appl. 5 (2) (2014) 73–80, https://doi.org/10.4236/msa.2014.52011.

[32] W. Khaliq, H.A. Khan, High temperature material properties of calcium aluminate cement concrete, Constr. Build. Mater. 94 (2015) 475–487, https://doi.org/10.1016/j.conbuildmat.2015.07.023.

[33] R.N. Edmonds, A.J. Majumdar, The hydration of monocalcium aluminate at different temperatures, Cem. Concr. Res. 1 (2) (1988) 12–17.

[34] R.N. Edmonds, A.J. Majumdar, The hydration of Secar 71 aluminous cement at different temperatures, Cem. Concr. Res. 19 (2) (1989) 289–294, https://doi.org/10.1016/0008-8846(89)90093-8.

[35] H. Pöllmann, Calcium aluminate cements - Raw materials, differences, hydration and properties. Rev. Mineral. Geochem., 74(Kiskyras 1960) (2012) 1–82. https://doi.org/10.2138/rmg.2012.74.1.

[36] C.E. Hughes, B. Walkley, L.J. Gardner, S.A. Walling, S.A. Bernal, D. Iuga, J.L. Provis, K.D.M. Harris, Exploiting in-situ solid-state NMR spectroscopy to probe the early stages of hydration of calcium aluminate cement, Solid State Nucl. Magn. Reson. 99 (January) (2019) 1–6, https://doi.org/10.1016/j.ssnmr.2019.01.003.

[37] M.A.L. Braulio, A.G.T. Martinez, A.P. Luz, C. Liebske, V.C. Pandolfelli, Basic slag attack of spinel-containing refractory castables, Ceram. Int. 37 (6) (2011) 1935–1945, https://doi.org/10.1016/j.ceramint.2011.02.007.

[38] J. Poirier, M. Rigaud, Corrosion of refractories: the fundamentals. F.I.R.E. compendium series, Göller Verlag, 2017. isbn: 9783872640062.

[39] B. Lothenbach, L. Pelletier-chaignat, F. Winnefeld, Stability in the system CaO - Al₂O₃ - H₂O, Cem. Concr. Res. 42 (12) (2012) 1621–1634, https://doi.org/10.1016/j.cemconres.2012.09.002.

[40] Z. Pan, J.G. Sanjayan, D.L.Y. Kong, Effect of aggregate size on spalling of geopolymer and Portland cement concretes subjected to elevated temperatures, Constr. Build. Mater. 36 (2012) 365–372, https://doi.org/10.1016/j.conbuildmat.2012.04.120.

[41] A. Abolhasani, H. Nazarpour, M. Dehestani, The fracture behavior and microstructure of calcium aluminate cement concrete with various water-cement ratios, Theoret. Appl. Fract. Mech. 109 (April) (2020) 102690, https://doi.org/10.1016/j.tafmec.2020.102690.

[42] G. Choe, G. Kim, M. Yoon, E. Hwang, J. Nam, N. Guncunski, Effect of moisture migration and water vapor pressure build-up with the heating rate on concrete spalling type, Cement Concr. Res. 116(August 2017) (2019) 1–10. https://doi.org/10.1016/j.cemconres.2018.10.021.

[43] N. Algourdin, P. Pliya, A.L. Beaucour, A. Simon, A. Noumowé, Influence of polypropylene and steel fibres on thermal spalling and physical-mechanical properties of concrete under different heating rates, Constr. Build. Mater. 259 (2020) 119690, https://doi.org/10.1016/j.conbuildmat.2020.119690.